JACS
JOURNAL OF THE AMERICAN CHEMICAL SOCIETY
pubs.acs.org/JACS
Article

Framework Short-Range Order Observed in a Spinel-Type Li Superionic Conductor

Yu Chen,[‡‡] Caleb Ramette,[‡‡] Matthew Krogstad, Maxim Avdeev, Erick Lawrence, Satya Kushwaha, Chao-Chun Wei, Rajavallipuram Sankaran Subramanian, Birender Singh, Bin Liu, Xiaoping Wang, Christina M. Hoffmann, Jue Liu, Paul Cardon, Kenneth S. Burch, Gopalakrishnan Sai Gautam, and Huiwen Ji*

Cite This: https://doi.org/10.1021/jacs.5c12231

ABSTRACT: Solid-state superionic conductors are characterized by rich structural disorders. Though structural complexities are central to their functionalities, they often give rise to short-range order that eludes detection by conventional diffraction-based techniques and is thus overlooked in establishing precise structure−property relationships. In this work, we synthesized single crystals of a recently discovered lithium (Li) superionic conductor $Li_{16.2(1)}In_{9.00(2)}Sn_{1.10(1)}O_{23.8}$ (LISO) for in-depth characterizations of structural subtleties. LISO exhibits an unusual spinel-like phase with significant Li overstoichiometry and a face-sharing Li network. Single-crystal neutron diffraction confirms significant Li disorder, as manifested in Li site splitting and partial occupancy. More importantly, synchrotron diffuse scattering combined with 3D-ΔPDF analysis and Monte Carlo simulations reveal short-range order in the nonalkali framework that might contribute to the phase stability and ionic conductivity. This work showcases an example in which subtle local energetics can be directly visualized in structurally disordered ionic conductors.

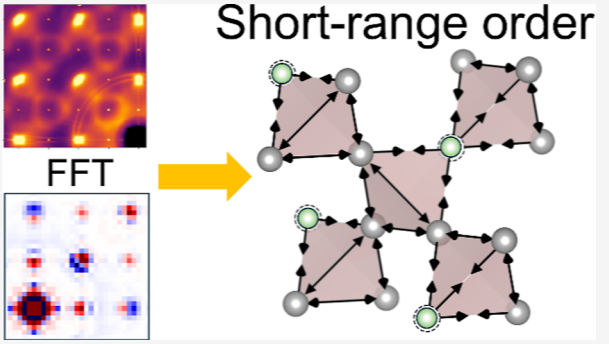

INTRODUCTION

There is currently an intense focus on developing alkali solid-state superionic conductors for use in all-solid-state batteries, with the promise of reduced flammability and greater energy and power density.[1−4] Despite the apparent diversity among material families exhibiting superionic conductivity, a high degree of structural disorder emerges as a unifying characteristic. Within the alkali-ion sublattice, disorder typically manifests through partial occupancy, significant thermal displacements, and site splitting,[4−6] creating an ensemble of ion configurations with comparable energies for easy migration.[7] The nonalkali framework sublattice, meanwhile, often exhibits rich substitutional and displacive disorder that play a key role in shaping the diffusion pathways and energy landscape of the alkali sublattice.[8−11] Accurately characterizing these subtle structural disorders and complexities is, therefore, essential for understanding ion transport mechanisms and guiding the design of next-generation superionic conductors.

Recently, a class of face-centered cubic (fcc) oxides, namely Li−In−Sn−O (LISO) that contains overstoichiometric Li (and more cations than anions) in a spinel-like structure, demonstrated Li superionic conductivity.[12] This unprecedentedly high ionic conductivity for the fcc structural family is achieved by incorporating excess Li into high-energy sites, forming face-sharing Li configurations with strong Coulombic repulsions. Consequently, facile ion motion is activated along these face-sharing Li pathways, as proven by ab initio molecular dynamics simulations, and is the origin of the observed >0.3 mS/cm room-temperature ionic conductivity and a remarkably low migration barrier of 255 meV.[12]

When LISO is synthesized in a powder form, nanodomains of a spinel-like phase coexist with a coherent cation-disordered rocksalt phase, with the former dominating the superionic conductivity. A schematic of the spinel crystal structure is shown in Figure 1a, in which the high-valent In/Sn occupies 16*d* while Li occupies 8*a* and 16*c*. Previous studies[12,13] have established that the spinel-like nanodomains form favorably in these Li-excess composition(s) to effectively separate Li and In/Sn. As a result, a continuous Li network composed of face-sharing 8*a* and 16*c* is formed (Figure 1b). Meanwhile, 8*b* remains empty to avoid unfavorable face sharing with high-valent In/Sn in 16*d*. On the other hand, the spinel-like phase is

Received: July 17, 2025
Revised: January 22, 2026
Accepted: January 26, 2026

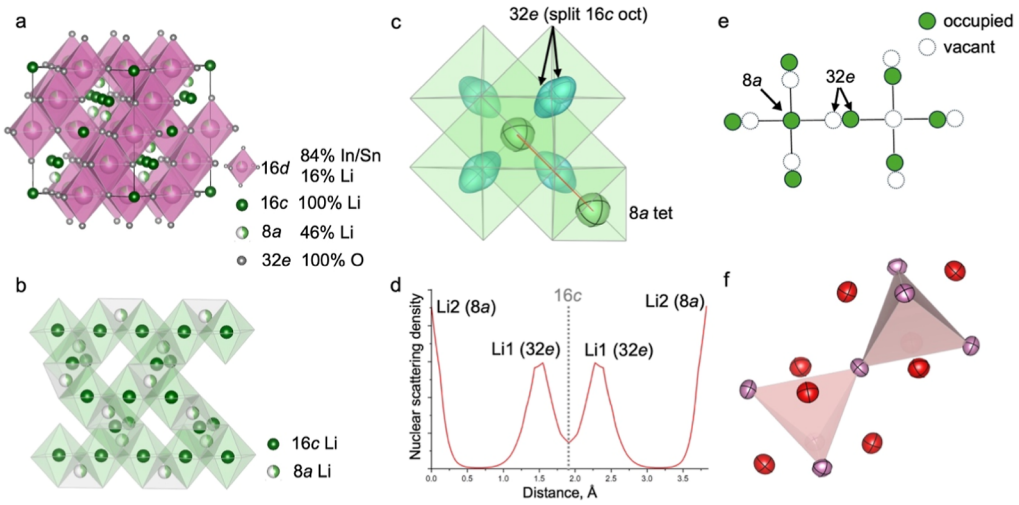

Figure 1. Average crystal structure derived from single-crystal diffraction. (a) Crystal structure of LISO. (b) Li network composed of face-sharing 8*a* and 16*c* sites. (c) Fragment of the crystal structure refined from neutron data highlighting 50% Li ADP ellipsoids in 8*a* and 32*e* sites, with Li density isosurfaces in a translucent cyan color. (d) Li nuclear density based on neutron diffraction along a Li2−Li1−Li1−Li2 path (red line in c). (e) Schematic of local Li site occupancy in 8*a* and 32*e*. (f) Structural fragment highlighting the 95% In (purple) and O (red) ADP ellipsoids, based on single-crystal XRD.

highly sensitive to synthesis conditions, especially the cooling rate and the starting Li content. It is kinetically trapped by coherent precipitation when cooled fast, resulting in the unique nanodomain microstructure in powders.[13] Upon prolonged heating, LISO readily loses excess Li and transforms to other types of cation order that suffocate the ion transport.[12] Though not exhaustively tested, the Li content in the spinel-like LISO phase (with the general formula $Li_xIn_9SnO_{15.5+x/2}$) has been observed to vary between 14.9[12] and 16.2 (this work), depending on the synthesis conditions. Therefore, the intricate interplay among stoichiometry, Li ion−ion repulsion, and framework cation order is critical for the overall stability of the phase. Some of these complex energetics might be reflected in short-range orders (SROs) that elude detection by conventional diffraction-based techniques.

Here, for in-depth characterizations of SROs, we grew LISO single crystals using the laser-diode floating zone method. The method combines fast cooling and seeded growth to yield single crystals of the metastable spinel-like phase. Unlike powder, single crystals allow diffuse scattering to be separated from Bragg reflections for the straightforward interpretation of SROs. While single-crystal neutron diffraction confirms the significant Li disorder as manifested in Li site splitting and partial occupancy, more importantly, our synchrotron total scattering shows highly structured diffuse scattering associated with SROs in the nonalkali framework. We interpreted such diffuse scattering using combined three-dimensional difference pair distribution function (3D-ΔPDF) analysis and Monte Carlo (MC) simulations.

RESULTS

Average Structure

Crystals grown from a nominal starting composition of $Li_{18.7}In_9SnO_{24.85}$ has a final composition of $Li_{16.2(1)}In_{9.00(2)}Sn_{1.10(1)}O_{23.8}$ as determined by elemental analysis (Table S1). This composition includes contributions from a minor Li_3InO_3 impurity, present at ∼3.9 wt % as determined by XRD refinement (Figure S2), which may slightly inflate the overall Li content. The O content is calculated based on charge balance. Unlike a conventional oxide spinel with a cation-to-anion ratio of 3:4, our material exhibits an unusual cation overstoichiometry with a cation-to-anion ratio close to 10:9. The ionic conductivity measured from a polished crystal piece containing multiple domains is 2.17×10^{-4} S/cm at 298 K with an Arrhenius-fit activation energy of 245(3) meV (Figure S1), comparable to the values reported based on a polycrystalline pellet.[12] Despite the presence of minor impurity, we selected monolithic domains of several hundred μm from the crystal boule for the subsequent experiments.

We first applied conventional diffraction techniques to investigate the Li site distribution in the target spinel phase. The neutron diffraction data were indexed to the $Fd\bar{3}m$ space group (Note 1 and Tables S2−S5). No additional Bragg reflections associated with a lower symmetry were observed. The refined average structure adopts a spinel-like order as shown in Figure 1a and agrees with a previous report based on polycrystalline LISO.[12] The tetrahedral 8*a* and octahedral 16*c* sites are exclusively occupied by Li at 46% and 100%, respectively, forming a 3D Li network (Figure 1b), while the octahedral 16*d* site is mixed with 84% In/Sn and 16% Li. No O vacancies were seen. Refinement also indicates that each 16*c* site is split into two 32*e* sites that are ∼0.7 Å apart (Figures 1c and S4). One of the two 32*e* sites is occupied by Li while the other is vacant. A maximum entropy method (MEM) analysis corroborates the site splitting, as is evidenced in the nuclear density distribution shown in Figure 1d. The 8*a* and 32*e* sites of Li thus adopt the same connectivity as in cubic Li-superionic garnets; i.e., each octahedral Li site is connected with two tetrahedral Li sites, while each tetrahedral Li site is connected with four octahedral Li sites. Same structural refinement and MEM analysis on the neutron diffraction data collected at 100 K yielded similar results (Tables S4, S5 and Figure S5), with no sign of global symmetry lowering upon cooling.

The refined Li occupancy in 16*c* and 8*a* indicates inevitable face-sharing repulsion. As a result, a 16*c* Li should shift away from an occupied 8*a* site or toward an unoccupied 8*a* site (Figure 1e), causing the observed 16*c* Li site splitting into two 32*e* sites. The site splitting is reminiscent of that seen in Li-rich

https://doi.org/10.1021/jacs.5c12231
J. Am. Chem. Soc. XXXX, XXX, XXX−XXX

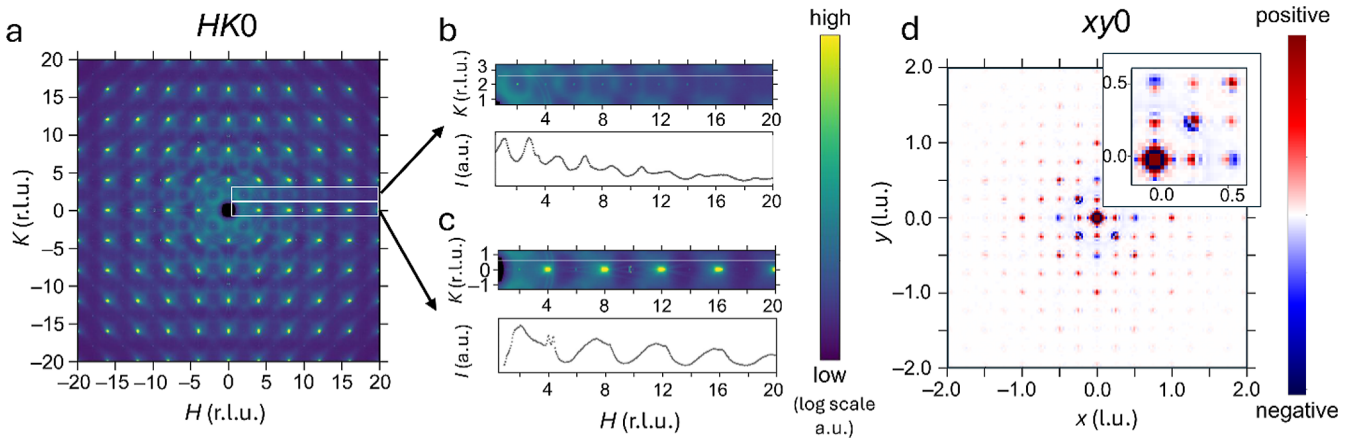

Figure 2. Symmetrized synchrotron X-ray total scattering and 3D-ΔPDF. (a) Total scattering in the *HK*0 plane at 300 K. (b) Zoom-in view of the square-shaped diffuse scattering in *HK*0 and integrated intensity between K = 2.55 and 2.65 along H (white line). (c) Enlarged view of the butterfly-shaped diffuse scattering in *HK*0 and integrated intensity between K = 0.55 and 0.65 along H (white line). (d) 3D-ΔPDF in the *xy*0 plane with a Bragg punch size of 0.2 r.l.u. at 300 K. Zoom-in view on the upper right corner.

superionic garnets,[14] e.g., the two split sites ~0.78 Å apart with each 42% occupied in the 48*g* octahedra in $Li_{6.5}La_3Zr_{1.5}Nb_{0.5}O_{12}$,[15] where Li−Li repulsion is significant.[16] Meanwhile, a 16*c* Li displaced away from one occupied 8*a* site will energetically penalize Li occupancy in the opposing 8*a* site. Therefore, an occupied tet-oct-tet Li cluster is unstable, which limits the 8*a* site occupancy to below 50%. This correlation is supported by a recent DFT study that demonstrates an 8*a* site occupancy >50% significantly destabilizes this spinel-like phase.[13]

Single-crystal XRD refinement yields noticeable anisotropic displacement parameters (ADPs) for the In/Sn atoms. In this material, since In and Sn (Z = 49, 50) are significantly heavier than O (Z = 8) or Li (Z = 3), X-ray is a more sensitive probe to In/Sn displacements than neutron (the neutron scattering length of In is weaker than that of O). Since no evidence of segregation between In and Sn was found, we refer to the 16*d* In/Sn mixed site as the In site hereafter. The In ADP ellipsoids are oblate, flattened along the body-diagonal of the cubic In_4O_4 cluster (Figure 1f). This indicates In displacements while keeping a rigid In−In bond length. This scenario is similar to the SiO_4 rotation in β-cristobalite[17] and the OA_4 rotation in some pyrochlores $A_2B_2O_7$[18,19] but is in contrast to the in/out displacements in some other pyrochlores like $Y_2Mo_2O_7$.[20,21]

Chemical SROs and a Local Size Effect

The complex energetics within the nonalkali framework leads to SROs, which give rise to elusive diffuse scattering alongside the well-defined Bragg reflections. The diffuse scattering and Bragg reflections constitute the so-called total scattering. The advantage of single-crystal total scattering over its powder analogue lies in the capability of separating diffuse scattering signals in 3D for a more straightforward interpretation.

The obtained synchrotron X-ray total scattering is shown in the *HK*0 plane at 300 K (Figure 2a). From this, two types of diffuse scattering were observed away from Bragg reflections. Both are 3D features that extend beyond the L = 0 plane. One type is square-shaped contours around the (4n + 2 4m + 2 0) Bragg reflections (n and m are integers), the intensity of which decays quickly toward higher $\mathbf{Q}$, as shown in the magnified view and the integrated intensity cut in Figure 2b. This type is reminiscent of similar reciprocal-space cuts for *fcc*-type Au−Cu alloys[22] and a class of cation-disordered rocksalts $LiMO_2$[8,23] (M is a trivalent metal). In both cases, these parts of the continuous 3D diffuse scattering contours originated from chemical SRO (also known as substitutional SRO). Here, the continuous contours have an uneven intensity around the square feature, which implies a displacive contribution on top of the chemical correlations. The second type of diffuse scattering is butterfly-shaped around the (4n 4m 0) Bragg spots. These features are asymmetric in intensity between the low-$\mathbf{Q}$ and the high-$\mathbf{Q}$ lobes. This type of diffuse scattering retains intensity to higher $\mathbf{Q}$'s than the first type, as shown in the magnified view and integrated intensity in Figure 2c. Such features are associated with local atomic displacements or the so-called atomic size effect,[24] which strongly manifests in ferroelectrics.[25] The atomic size effect, or local size effect, originally refers to the phenomenon in a solid solution in which atoms of different sizes cause variations in neighbor distances. The effect causes characteristic asymmetric diffuse scattering. Finally, the presence of (4n + 2 0 0) or equivalent reflections that are forbidden for $Fd\bar{3}m$ indicates subtle symmetry breaking, although their intensities are 3−4 orders of magnitude lower than the allowed Bragg spots.

Diffuse scattering away from Bragg spots comes from SROs in the vicinity of atoms; we thus turn to 3D-ΔPDF to extract correlations between immediate atomic neighbors. We used a "punch-and-fill" method[26] to remove Bragg spots at all integer *HKL*s. The remaining diffuse scattering went through Fourier transform to real space. The resulting 3D-ΔPDF, a Patterson function, shows deviation from the average structure. The *xy*0 section of 3D-ΔPDF is shown in Figure 2d. Positive (red) and negative (blue) intensities correspond to increased and decreased scattering densities, respectively, in the interatomic vectors.

In 3D-ΔPDF, net intensity in vectors indicates chemical SRO. Positive intensity indicates higher or heavier-metal site occupancy, while negative intensity indicates the opposite. Here, the most significant chemical SROs are seen at <±1/4, ±1/4, 0>, <±1/2, ±1/2, 0>, and <±1/2, 0, 0> (or <0, ±1/2, 0>), from a zoom-in view in Figure 2d. Since X-ray is more sensitive to In than to O or Li, they indicate SROs in In-containing metal−metal pairs, as depicted in Figure S6. The negative intensity at <±1/4, ±1/4, 0> indicate that for nearest-neighbor (NN) metal correlations, In−Li pairs are favored over In−In pairs. Likewise, the net negative intensity at <±1/2,

https://doi.org/10.1021/jacs.5c12231
J. Am. Chem. Soc. XXXX, XXX, XXX−XXX

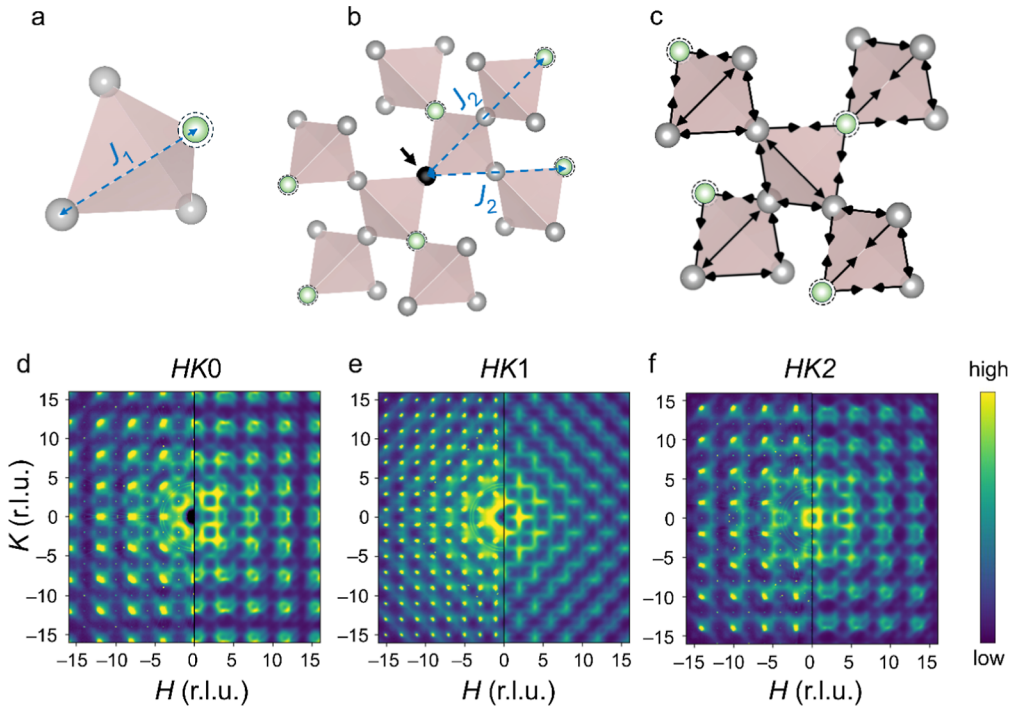

Figure 3. Simulations of chemical SROs and the local size effect. (a–c) Modeled correlations among 16*d* sites. Representative metal pairs at (a) <±1/4, ±1/4, 0> and at (b) <±1/2, ±1/2, 0> with the characteristic chemical correlations, highlighted by blue dashed lines. Both energy terms J_1 and J_2 are positive, which lead to negative chemical correlations. Solid gray and smaller green spheres are In-occupied and Li-substituted sites, respectively. In (b), a representative In-occupied reference site is highlighted in black. (c) Size effect involving an elongated In–In distance and a shrunk In–Li distance with arrows pointing in the directions of displacements. Experimental observations (left) and MC-simulated diffuse scattering patterns (right) in (d) *HK*0, (e) *HK*1, and (f) *HK*2, intensity on a log scale.

0, 0> and <0, ±1/2, 0> suggests that In–Li is favored over In–In for metal pairs across 16*c* and 16*d*. Finally, the net intensity at <±1/2, ±1/2, 0> is highly sensitive to the Bragg punch size selected: a smaller punch (Figure 2d) yields positive correlation (favoring In–In), whereas a larger one yields negative when the corresponding square-like diffuse scattering is better isolated (favoring In–Li) (Figure S9a,b).

Besides chemical SROs, vectors at <±1/4, ±1/4, 0> show a bimodal intensity distribution, a maximum shifted away from the origin and a minimum toward the origin (Figure 2d). Such features indicate a local size effect and atomic displacements. In this case, the correlations indicate the heavier NN In–In are displaced farther apart while NN In–Li pairs are displaced closer. Vectors at <±1/4, 0, 0> and <0, ±1/4, 0> behave the opposite, with a maximum shifted toward the origin and a minimum shifted away. These vectors are from immediate O–In/Sn and O–Li bonds, respectively, and suggest that the O–In/Sn bond length is smaller than the average metal-O bonds and spans a range. Because the split intensities are higher for <±1/4, ±1/4, 0>, we expect this size effect to be the dominant origin of the butterfly-shaped diffuse scattering.

Three major SROs, i.e., two chemical SROs at <±1/4, ±1/4, 0> and <±1/2, ±1/2, 0> plus one size effect at <±1/4, ±1/4, 0>, were incorporated to construct a Monte Carlo (MC) model, as shown in Figure 3a–c. Only the involved 16*d* sites are shown. The signs and relative dominance of the correlations were determined by comparing simulated patterns, as shown in Figures S7, S8 and Note 2. Final parameters that allow the closest resemblance to observation are provided in Methods. Figure 3a,b illustrates the negative chemical correlations, i.e., preferred In–Li instead of In–In occurrences, in the <±1/4, ±1/4, 0> and <±1/2, ±1/2, 0> metal–metal pairs. Note that a negative chemical correlation is equivalent to a positive interaction energy *J* between alike atoms. Figure 3c depicts the size effect, i.e., longer NN In–In distances and shorter NN In–Li distances. Chemical SROs and the size effect can be modeled individually (Figures S10 and S11) or combined, as shown in Figure 3d–f. The constructed model closely reproduces experimental observation and matches the square-like and asymmetric butterfly-like features in both shape and relative intensity. The simulation of *HK*1 shows a clear staircase feature, whereas the corresponding observed zone image shows it more subtly. This discrepancy is either due to a very intricate balance between the modeled parameters or more subtle parameter(s) that are not captured in the modeling. 3D-ΔPDF of the model matches the most outstanding chemical SROs at <1/4, 1/4, 0> and <1/2, 1/2, 0> in the observation (see comparison in Figure S9b,c). The negative net correlation at <1/2, 0, 0> is missing from the model because the model assumes In in 16*d* only and therefore contains no chemical SROs at this vector. The size effect at <1/4, 1/4, 0> is also reproduced. However, the model misses the observed bimodal splitting at <1/4, 0, 0>. This is possibly due to the smaller ionic size of Sn^{4+} than of In^{3+}, which is not considered in the model.

Beyond the immediate atomic pairs, over a longer range, collective displacements in 3D-ΔPDF are observed and manifested especially when a smaller punch size is used (Figure S9d–g). Such 3D-ΔPDF signals must come from near-Bragg diffuse scattering, which call for further analysis.

https://doi.org/10.1021/jacs.5c12231
J. Am. Chem. Soc. XXXX, XXX, XXX–XXX

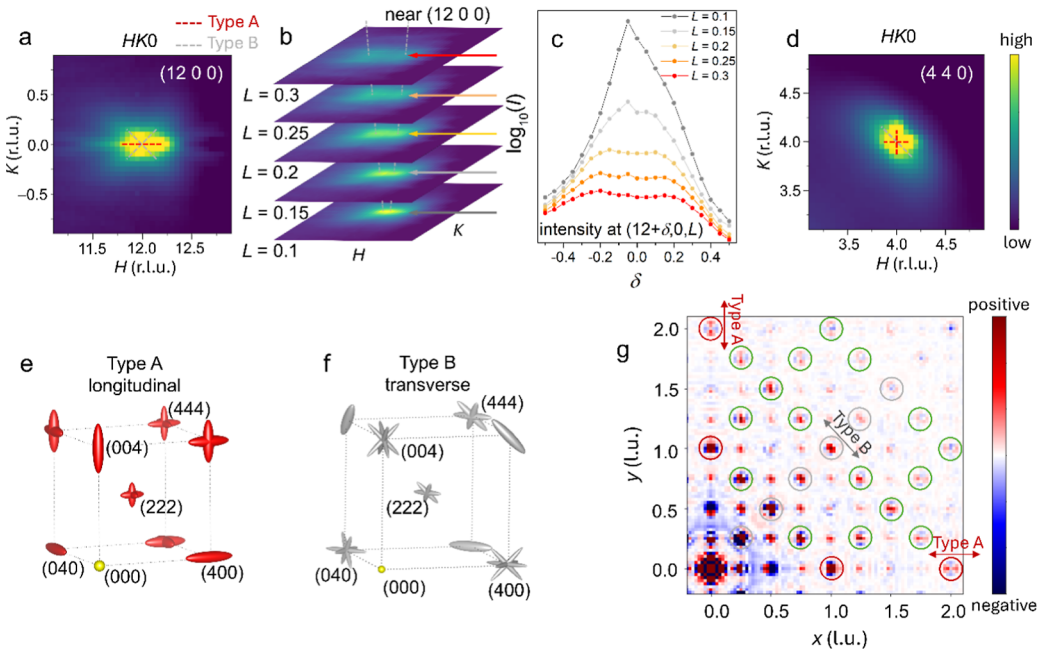

Figure 4. Near-Bragg diffuse scattering reveals collective displacements. (a) Total scattering intensity near (12 0 0) in *HK*0. Types A and B diffuse scattering are indicated by red and gray dashed lines, respectively. (b) Reciprocal space views above (12 0 0) in *L* planes. (c) Total scattering intensity along *H* paths as marked by arrows with corresponding colors in (b). (d) Scattering intensity near (4 4 0) in *HK*0. Summarized distribution of (e) Type A and (f) Type B diffuse scattering. (g) 3D-ΔPDF in *xy*0 at 300 K with a radius of 0.2 r.l.u. Bragg punch. Red, gray, and green circles highlight displacements of predominantly longitudinal, transverse, and mixed origins, respectively.

Near-Bragg Diffuse Scattering and Collective Displacements

It is established in diffraction theory that near-Bragg, small-$\boldsymbol{q}$ diffuse scattering indicates collective displacements, often referred to as strain or a displacement field.[27] $\boldsymbol{q}$ is a wavevector in reciprocal-space, originating from Bragg. In principle, streaky diffuse scattering through Bragg peaks can also arise from occupational disorder, including 1D (e.g., the alkali-vacancy short-range order in hollandite tunnels[28]) and 2D scenarios (e.g., stacking faults in layered crystal structures[29]). However, such an origin is less likely in the present case given the absence of any obvious 1D or 2D structural motifs and the fact that the diffuse streaks are concentrated around the Bragg reflections. In LISO, two types of near-Bragg diffuse scatterings are observed. They appear throughout the entire reciprocal space, and we showcase a few examples below to make the point.

The first type, termed Type A, is 1D diffuse scattering rods along the ⟨100⟩ directions. An example is highlighted by a red dashed line near (12 0 0) in the [100] direction, as shown in Figure 4a. The rod is noticeably stronger for its high-$\boldsymbol{Q}$ lobe. The second type, termed Type B, is also 1D rods but in ⟨110⟩ directions, e.g., along [110] and [1$\bar{1}$0] near (12 0 0) as marked by gray dashed lines. Near the same Bragg, more Type B diffuse scattering rods are seen above the *HK*0 plane. As shown in Figure 4b, two diffuse blobs that gradually shift apart toward a higher *L* are observed. They are intersections of the [101] and [$\bar{1}$01] rods with the *L* planes and are corroborated by the widening peak splitting in the total scattering intensity mapping shown in Figure 4c.

The 1D diffuse rods suggest correlations in the corresponding directions between 2D planes. With cubic symmetry, the rods should adopt 3 ⟨100⟩ and 6 ⟨110⟩ equivalent branches for Types A and B, respectively. However, when extending from certain Bragg peaks, particularly those along high-symmetry directions, systematic absences are observed. In Figure 4a for Bragg (12 0 0) and in Figure S12 for (8 0 0) and (16 0 0), Bragg spots on the *H* axis show Type A diffuse rods along [100] only and Type B rods along [110], [$\bar{1}$10], [101], and [$\bar{1}$01]. Along face-diagonals, e.g., (4 4 0) in Figure 4d and (8 8 0), (12 12 0) in Figure S13, the [$\bar{1}$10] branch is dominant for Type B and only the [100] and [010] branches are seen for Type A. Along body-diagonals, e.g., (2 2 2), (4 4 4), (8 8 8) in Figure S14, located on a 3-fold rotation axis, all three ⟨100⟩ branches are seen for Type A while only three branches, i.e., [$\bar{1}$10], [$\bar{1}$01], and [0$\bar{1}$1], are seen for Type B. For Bragg spots away from these major directions, the diffuse scattering rods show gradual shift in dominance (Figure S15). Note that these diffuse scattering features are more spread out toward higher $\boldsymbol{Q}$ space (Figures S12−S14), consistent with the displacive nature of the associated SROs.

The observed absences of diffuse scattering rods are summarized in Figure 4e,f. They reveal the nature of displacements following the intensity equation $I(\boldsymbol{q}) \propto |\boldsymbol{G}\cdot \boldsymbol{u}(\boldsymbol{q})|^2$, wherein $\boldsymbol{G}$, $\boldsymbol{q}$, and $\boldsymbol{u}$ are the Bragg, reciprocal-space wavevectors, and real-space displacement vector, respectively. For Type A, the displacements must be longitudinal, i.e., $\boldsymbol{u}(\boldsymbol{q})//\boldsymbol{q}$. This explains why the $\boldsymbol{q} = \delta[010]$ and $\boldsymbol{q} = \delta[001]$ rods are absent near (400) because the corresponding $\boldsymbol{G}$ does not contain any *K* or *L* components; near (444), all three rods along [100], [010], and [001] show up. Meanwhile, for Type B, the $\boldsymbol{u}$ displacements must be in a transverse mode, i.e., $\boldsymbol{u}(\boldsymbol{q})\perp\boldsymbol{q}$. This explains why the $\boldsymbol{q} = \delta[110]$ rod near (440) is absent (Figure 4d), as is the corresponding $\boldsymbol{u}(\boldsymbol{q})\perp[110]$ (or $\boldsymbol{G}$). Near Bragg (400), the $\boldsymbol{q} = \delta[011]$ (or $\delta[0\bar{1}1]$) rod is absent. This is possible only if the corresponding $\boldsymbol{u}$ displacements are perpendicular to both $\boldsymbol{q}$ and $\boldsymbol{G}$. In other

https://doi.org/10.1021/jacs.5c12231
J. Am. Chem. Soc. XXXX, XXX, XXX−XXX

words, the u's must be along $[0\bar{1}1]$ (or $[011]$) for the $q = \delta[011]$ (or $\delta[0\bar{1}1]$) modes.

The inferred collective displacements indeed show up in the 3D-ΔPDF (Figure 4g). Vectors that map to heavy In−In correlations (circled) have the strongest signals. All displacive q modes contribute by $u(r) = \sum_q u(q \cdot r)$, wherein r is the real-space vector. One thus expects a certain q to dominate if it is parallel to r. In Figure 4g, for the ΔPDF vectors along x (red circles), longitudinal mode $q = \delta[100]//x$ should dominate. Indeed, extended or split positive ΔPDF intensity in the x direction is seen, e.g., near the <2, 0, 0> vector. Likewise, the ΔPDF vectors on y have dominant longitudinal displacements in the y direction. On the other hand, for vectors in the [110] face-diagonal direction (gray circles), e.g., <1/2, 1/2, 0>, <1, 1, 0>, a Type B transverse mode of $q = \delta[110]$ dominates, causing the positive ΔPDF intensity to extend or split in the $[1\bar{1}0]$ direction. Other ΔPDF vectors (green circles) show displacements contributed by all q's with a gradual shift in dominance. Since the collective displacements in 3D-ΔPDF come from near-Bragg diffuse scattering, their appearance is sensitive to the Bragg puncher size used. If the punch size increases to remove the near-Bragg diffuse scattering prior to the Fourier transform, such 3D-ΔPDF features disappear (Figure S16).

Given the collective displacements, we turned to micro-Raman spectroscopy to investigate if there is a symmetry lowering of the single crystals. From the factor-group analysis for the $Fd\bar{3}m$ space group, we expect to see phonon modes of A_{1g}, E_g, and T_{2g} symmetry from the (001) plane. Figure S17a,b shows the Raman spectra in the parallel (XX) and crossed (XY) polarization configuration. The Raman spectra show the detection of the phonon mode at 12.7, 18.6, 41.0, and 66.1 meV. Similar results were obtained across multiple locations on several crystals. The angle-resolved Raman measurements of the phonon modes in XX and XY polarization configurations is shown in Figure S17c,d. The observed angular dependence of the phonon modes indeed reveals the expected symmetry of the modes at 12.7 meV (T_{2g}), 18.6 meV (T_{2g}), 41.0 meV (E_g), and 66.1 meV (A_{1g}, E_g) as shown in Figure S18. No new mode emerges, indicating that the crystal symmetry remains cubic down to μm resolution. It suggests that the symmetry lowering, if any, due to the collective displacements is within domains much smaller than the laser spot size of ∼2 μm. This is consistent with the estimated correlation lengths, ∼4.7 l.u. (∼4.1 nm) and ∼9.6 l.u. (∼8.4 nm) for Type A and Type B displacements, respectively, based on a Lorentzian fit (Figures S19 and S20). Infrared spectroscopy would be a complementary technique to Raman spectroscopy and can be more sensitive to asymmetric structural distortions. But given the limited selection rules, the detection of the distortion confined to small domains and/or broken inversion symmetry likely remains difficult.

DISCUSSION

While the disorder of the Li sublattice is visualized by the Li nuclear density distribution based on average structure characterization using neutron diffraction, the SROs in the nonalkali framework of LISO were captured by X-ray total scattering, which reveal the complex energetics experienced by the lattice. Diffuse scattering of both chemical and displacive origins is observed. The chemical SROs are similar to those observed in Cu−Au alloys[22] and cation-disordered $LiMO_2$,[30,31] which are likely developed to maintain local charge neutrality and maximize the configurational entropy. The positive energy terms J_1 and J_2 between 16d sites that are <±1/4, ±1/4, 0> and <±1/2, ±1/2, 0> apart are electrostatic energy if local metal clusters break charge neutrality. Specifically, a positive J_1 and the resultant preferred nearest In−Li pairs dictates four nearest 16d sites that form a tetrahedron to be either In_4 or In_3Li; J_2 regulates bigger clusters across multiple such tetrahedra. The J_1 and J_2 values, if projected onto realistic synthesis conditions, are on the order of several tens of meV, comparable to the effective cluster interactions reported for other well-established substitutional systems.[32,33] X-ray scattering and 3D-ΔPDF detect pairwise correlations, which is a result of these local metal clusters favored by charge neutrality. The ratio of J_1 and J_2 should be a function of the site mixing ratio of Li and In. Similar effects were seen in $(Bi,Zn)_2(Zn,Nb)_2O_7$ pyrochlores.[34] Note that though charge neutrality has long been regarded as a rule for phase stability, recent studies reveal that local charge imbalances can arise in ionic conductors to create local polarization and modulate ion transport.[35] Meanwhile, the repulsive Li−Li interactions between the face-sharing 8a and 16c sites expand the lattice, necessitating a bulky metal in the framework, i.e., In^{3+} with a radius of 0.80 Å. A local size effect is thus developed to relieve strains. This is because the 16d In sites form a network of tetrahedral In_4 clusters. Within the cluster, each In shares its O_6 octahedral edges with three nearby In ions. The bulky In^{3+} might be insufficiently screened by O and experiences repulsion from nearby In, causing elongation of the In−In bond. Furthermore, by DFT calculations (Supporting Information, Note 4 and Figure S21), we reveal that such structural distortion can lead to a more continuous distribution of Li site energies within the spinel-like structure, thereby facilitating a flat energy landscape for facile Li-ion motion. Thus, structural framework distortion may provide the additional benefit of enhancing Li-ion conductivity.

The stability of the spinel-like phase is highly sensitive to the framework chemistry, as suggested by additional powder synthesis (Figures S22−S24 and Note 5). The calcined powder LISO has different phase components, i.e., containing the target spinel-like phase (35.5 wt %) and a coexisting cation-disordered rocksalt (DRX) phase (64.5 wt %),[12] from single crystals (Figure S2). A mere 5% substitution of Sc for In results in separated $LiInO_2$ (γ-$LiFeO_2$-type) and Li_3InO_3 phases, whose Li conductivity falls below the detection limit, without a trace of the target. Previous studies have established that, despite the same O sublattice, the fraction of percolating Li pathways is significantly enhanced for a spinel-like cation order, compared with a DRX order, and severely suppressed for a γ-$LiFeO_2$-type order.[36] Meanwhile, replacing the minor component Sn with Ti retains a major spinel-like phase, while doing the same with isoelectronic Zr does not. Substitution of higher-valent Nb results in a small fraction of the target phase (13.6 wt %) mixed with side phases. These results do not support a straightforward correlation between phase stability and apparent attributes like size and charge, especially considering the stark contrast between the results of isoelectronic substitution of Ti^{4+} (0.605 Å) for Sn^{4+} (0.69 Å) and Sc^{3+} (0.745 Å) for In^{3+} (0.8 Å). Given the local displacements of In observed in synchrotron diffuse scattering which is a result of energy lowering in the structure, one might speculate that the synthesizability of this cation-overstoichiometric spinel-like phase is correlated with the framework cation's ability to locally distort. Indeed, InO_6 and SnO_6

https://doi.org/10.1021/jacs.5c12231
J. Am. Chem. Soc. XXXX, XXX, XXX−XXX

octahedral distortion has been reported in Sn-doped indium oxide and $In_4Sn_3O_{12}$.[37] Among the substituting TMs, Ti^{4+} and Nb^{5+} are also known as d^0 distorters, while Zr^{4+} and Sc^{3+} rarely show any tendency to distort off center in coordination octahedra.[38,39] To verify this correlation, however, local O displacements need to be precisely characterized by using neutron diffuse scattering before a solid conclusion can be made about local In/Sn−O bond deviations.

Despite the different synthesis conditions and apparent phase compositions of crystal and powder samples of LISO, their measured ionic conductivities and activation energies are comparable (Figure S1). One possible explanation is that the rocksalt phase observed for powder samples is also spinel-like at the short-range. This would be consistent with our recent work showing that the spinel-like phase forms coherently within the rocksalt matrix upon fast cooling.[13] Perhaps the directional cooling inherent to floating zone synthesis enabled the much larger domains in crystal samples and allowed us to perform in-depth structural analysis, while such a condition is absent during powder synthesis. Nonetheless, given the comparable performance of powder and crystal samples, there is strong promise that industrial-scale powder synthesis can deliver consistent performance provided that the initial Li content is controlled and the cooling rate is sufficiently rapid (e.g., via spray pyrolysis).

The relationship between the local size effect and the collective displacements is worth understanding. Collective displacements originate from multibody interactions. In LISO, the In_4 tetrahedra are connected through corners, forming a network similar to the SiO_4 network in β-cristobalite[17] and the OBi_4 network in $Bi_2Ru_2O_{7-\delta}$.[18] In the latter two cases, the SiO_4 and OBi_4 tetrahedra are locally more expanded than dictated by the average structure. But because of the connectivity through all corners, the tetrahedra cannot independently expand and have to undergo concerted rotation, known as rigid-unit modes (RUMs).[40,41] Such rigid constraints likely also exist in LISO. In other words, the local size effect might cause the concerted rotation of In_4 tetrahedra to create collective displacements. Indeed, an MC model with a pure size effect yields sharp ⟨110⟩ streaks from Bragg spots, resembling the Type B near-Bragg diffuse scattering rods observed (Note 3 and Figure S26a). This model assumes no Li substitution in 16*d* and, therefore, no chemical SROs. Accordingly, the modeled 3D-ΔPDF shows dominant transverse displacements for atomic pairs in face-diagonal directions (Figure S26b). It indicates that the collective transverse displacements originate from the local size effect. In reality, the Type B diffuse scattering features observed are not as sharp as modeled, likely due to the 15% Li for In substitution in the 16*d* network. This substitution breaks the local connection, reduces the correlation length, and might convert dynamic modes to static glassy disorder. Since the synchrotron scattering method we applied does not have energy resolution, it is unclear whether the collective displacements are static or dynamic (e.g., from acoustic phonon modes). This will be a question that will motivate future inelastic neutron or X-ray scattering studies. The longitudinal displacements associated with Type A diffuse scattering, on the other hand, seem unrelated to the size effect. This is because their characteristic signals do not appear in the pure size-effect MC model (Figure S26b). Type A diffuse scattering also shows unique asymmetry between the high- and low-**Q** lobes in a diffuse rod. The asymmetry resembles that of strain fields in alloys containing lattice-coherent precipitation.[42] Similar coherent precipitation might appear in LISO crystals due to metastable order−disorder transition, which was previously observed in powder LISO samples.[13]

CONCLUSIONS

In summary, we investigated the structural short-range orders (SROs) in a recently discovered cation-overstoichiometric spinel-like Li superionic conductor using single crystals. Significant disorder in the Li sublattice as manifested in site splitting and partial occupancy was confirmed by neutron diffraction. More importantly, our synchrotron total scattering shows highly structured diffuse scattering associated with SROs in the nonalkali framework. 3D-ΔPDF and Monte Carlo simulations were combined to explain the diffuse scattering observed. We identified chemical SROs as well as a local size effect; i.e., the nearest In−In pairs are displaced farther apart while the nearest In−Li pairs are displaced closer together. The observed SRO might affect the phase stability and Li-ion conductivity. Near-Bragg diffuse scattering was also observed to suggest the presence of strain fields in the material. This work showcases an example in which subtle local energetics can be directly visualized. We envision that future characterizations capturing these structural subtleties could reveal previously overlooked structure−property relationships in ionic conductors.

EXPERIMENTAL METHODS

Crystal Growth and Preliminary Characterizations

Li_2CO_3 (≥99.9%, Sigma-Aldrich), In_2O_3 (99.999%, MSE Supplies), and SnO_2 (99.9%, Sigma-Aldrich) were weighed in a molar ratio of 9.35:4.50:1. The specific In/Sn ratio was selected based on the most ionically conductive composition identified in the series. Regarding the impact of the In/Sn ratio on ionic conductivity, readers are encouraged to refer to prior works.[12,13] The precursors were mixed in a zirconia jar using a GELON GN-360 planetary ball mill at 180 rpm for 12 h. The powder was pelletized and sintered at 873 K in air for 24 h. Seed and feed rods approximately 7 mm in diameter were prepared from the sintered powder by using a hydrostatic press at 65 MPa of pressure. The rods were sintered for 8 h at 973 K. A laser diode floating zone furnace (Crystal Systems Corporation, available at the PARADIM Facility at JHU) with five near-IR lasers (974 nm) in horizontal geometry was used to grow single crystals. The seed and feed rods were translated at a rate of 10 and 15 mm/h, respectively, which was varied as needed during growth to stabilize the molten zone. The rotation of the rods was antiparallel at 10 rpm. A mixed atmosphere of Ar with a flow rate of 0.25 L/min and O_2 with a flow rate of 2 L/min was applied. The flow rate was optimized to aid in controlling the severe Li loss from the melt and retain optical transmission through the sample chamber by reducing the vapor coating. The O_2 was added to control the oxidation states of In and Sn during growth.

Single-crystal X-ray diffraction was collected on a Rigaku XtaLAB Synergy-R high-flux rotating anode diffractometer at room temperature. Data analysis was carried out using SHELXLE. Powder XRD was performed on the ground single crystals using a STOE STADI P diffractometer in transmission geometry with Mo Kα1 radiation and refined with the GSAS-II package. EDX was performed using an FEI TENEO SEM equipped with an EDAX Octane Elect EDS/EDX System. *T*-variant ionic conductivity was measured from a polished crystal piece (0.0221 cm^2 in area, 0.080 cm in thickness) containing multiple domains by using sputtered gold as blocking electrodes.

Single-Crystal Neutron Diffraction and Data Analysis

Time-of-flight single-crystal diffraction data were collected on TOPAZ at the Spallation Neutron Source (SNS), ORNL, at both

https://doi.org/10.1021/jacs.5c12231
J. Am. Chem. Soc. XXXX, XXX, XXX−XXX

100 and 300 K. The TOPAZ neutron diffraction analysis was performed with Jana2020, version 1.3.58.[43] Extinction was corrected using the Type 1 isotropic Lorentzian model of Becker and Coppens.[44] In and Sn atoms were placed in the 16*d* site, and their occupancies were constrained to have a 9:1.1 ratio. The remaining occupancy was allocated to Li under the constraint of maintaining the overall occupancy of the 16*d* site at 1. The occupancy of the Li 32*e* site was found to refine slightly above 0.5 and then was fixed to 0.5. The occupancy of the Li 8*a* site was set in Jana to be calculated via an equation to maintain the overall neutral charge balance. Jana2020 was also used to prepare the input files for Dysnomia[45] to perform analysis of the neutron scattering density distribution with the Maximum Entropy Method. Visualization of the isosurfaces and calculations of 1D density profiles were done with VESTA.[46]

Synchrotron Total Scattering

Room-temperature single-crystal diffuse X-ray scattering data from LISO were collected at the P21.1 beamline at PETRA III. Monochromatic X-rays with incident energy 101.64 keV were scattered from the sample in transmission, with scattered X-rays counted by a Dectris Pilatus 2M CdTe area detector. The sample was rotated over a 371.85° range with images read out every 0.1005° as the crystal was continuously rotated at 0.1°/s. Three scans were taken with slightly different detector positions to account for gaps between sensor chips in the detector. Images were stacked into three-dimensional arrays, processed and aligned using NXRefine,[47] and transformed into oriented reciprocal space using CCTW.[48]

3D-ΔPDF

Single-crystal diffuse scattering data from LISO were symmetrized by using all cubic operations. A "punch-and-fill" procedure was then applied to remove all Bragg peaks, removing all data within a radius 0.14 $Å^{-1}$ (or otherwise specified in the text) around Bragg positions[49] (all integer HKLs whether or not systematic absence is expected based on the space group) and filling these areas using Gaussian interpolation.[50] A Tukey window was applied prior to the fast Fourier transform (FFT) to reduce leakage artifacts.

X-ray Diffuse Scattering Modeling

A domain of 25 × 25 × 25 spinel unit cells was used for the modeling of X-ray diffuse scattering using the DISCUS SUITE package.[51] The simulated patterns are generated by subtracting 50% of the Bragg peak intensity. When setting up the unit cell, all Li atoms in the 8*a* site are omitted as there are no 3D-ΔPDF correlations involving the site. The 16*d* site is randomly occupied by 85% In and 15% Li to start with, while 16*c* is fully occupied by Li. Since X-ray cannot differentiate In from Sn, all Sn atoms are treated as In. All Monte Carlo modeling was performed for the 16*d* site. The diffuse scattering due to chemical and displacive SRO are simulated in two separate steps or then combined.

The chemical SRO was modeled using the Monte Carlo energy taking the following Ising-type form at an effective temperature of 5 *kT* to allow thermal fluctuations that better reproduce the observation

$$E = \sum_{r\in\{16d\}} \sum_{r'\in\{\pm\frac{1}{4},\pm\frac{1}{4},0\}} J_1\sigma_r\sigma_{r+r'} + \sum_{r\in\{16d\}} \sum_{r'\in\{\pm\frac{1}{2},\pm\frac{1}{2},0\}} J_2\sigma_r\sigma_{r+r'}$$

wherein various J_1 and J_2 values were tested with $J_1 = 0.15T$ and $J_2 = 0.12T$ being selected for yielding high resemblance to observation. T is the effective temperature and $\sigma = 1$ or 0 depending on whether the site is occupied by In or Li, respectively. If we assume that, upon cooling from a melt during crystal growth, atoms freeze at ∼1000 °C, then our chosen J_1 and J_2 values are roughly 65−80 meV.

The displacive SRO was modeled using a standard Lennard-Jones potential at an effective temperature of 0.8 *kT*

$$\begin{aligned} E' = & \sum_{\text{In}} \sum_{\text{In(NN)}} D_1\left[\left(\frac{d_{\text{In-In}}}{d}\right)^{12} - 2\left(\frac{d_{\text{In-In}}}{d}\right)^{6}\right] \\ & + \sum_{\text{In}} \sum_{\text{Li(NN)}} D_2\left[\left(\frac{d_{\text{In-Li}}}{d'}\right)^{12} - 2\left(\frac{d_{\text{In-Li}}}{d'}\right)^{6}\right] \\ & + \sum_{\text{In}} \sum_{\text{O(NN)}} D_3\left[\left(\frac{d_{\text{In-O}}}{r}\right)^{12} - 2\left(\frac{d_{\text{In-O}}}{r}\right)^{6}\right] \\ & + \sum_{\text{Li}} \sum_{\text{O(NN)}} D_4\left[\left(\frac{d_{\text{Li-O}}}{r'}\right)^{12} - 2\left(\frac{d_{\text{Li-O}}}{r'}\right)^{6}\right] \\ & + \sum_{\text{In}} \sum_{\text{O(NN)}} \sum_{\text{In(NN)}} K[\alpha_{\text{In-O-In}} - \alpha_0]^2 \end{aligned}$$

wherein the first two main terms model the desired NN In−In and In−Li distances, i.e., the size effect, the third and the fourth terms constrain the In−O and Li−O bond lengths relatively close to the ideal structure, and the last term keeps the nearest In−O−In angle close to 90°. The target $d_{\text{In-In}}$ and $d_{\text{In-Li}}$ values were systematically varied and finally set at 102% and 98% of the ideal value, i.e., $\frac{\sqrt{2}}{4}\times$ (lattice dimension), respectively, for yielding high resemblance to observation. D_1 and D_2 are the potential depth and are both set at −400 *kT*. The target $d_{\text{In-O}}$ and $d_{\text{Li-O}}$ are set at the ideal value, i.e., $\frac{1}{4}\times$ (lattice dimension). D_3 and D_4 are both set at −50 *kT*. The force constant K is set at 50 *kT* and the target angle α_0 is set at 90°. The potential depths D_1 and D_2 were intentionally set to be 1 order of magnitude larger than the remaining terms because their corresponding pairwise correlations produce the strongest signals in synchrotron X-ray-based 3D-ΔPDF measurements. The other potential depths were chosen to preserve physically reasonable first-coordination metal−oxygen bond lengths and angles, and these pairs do not produce strong X-ray 3D-ΔPDF signals. At room temperature, the values of D_1 and D_2 are approximately 10 eV, which lies at the upper end of the typical binding energy range of a few eV reported for solids.[52]

Though In and Sn are indistinguishable under X-ray scattering, their significantly different ionic radii and oxidation states will likely lead to additional SRO. For example, driven by charge balance, Li might preferably substitute next to Sn in 16*d*; the smaller size of Sn in comparison to In might disrupt the otherwise consistently longer nearest In−In distances. These effects are not considered in the model.

Raman Scattering

The Raman scattering measurements were performed via a custom-built low-temperature Raman setup[53] in the backscattering configuration using 532 nm (2.33 eV) excitation laser at low power (≤0.1 mW) to avoid any local heating effects. A 100× objective with a spot size of ∼2 μm in diameter was used to focus the laser on the sample. The spectra were dispersed using 1200 lines/mm grating, and the dispersed light was collected with an Andor CCD. The angle-resolved Raman measurements were performed using linear polarized light with controlling the incident and scattered light polarization using half wave plates, and a fixed analyzer was used to analyze the scattered light polarization. The dark counts were removed by subtracting the collected data with the same integration time with blocking of the laser. All of the Raman measurements presented in this work were performed at room temperature.

Polycrystalline Sample Synthesis

Polycrystalline LITO, LIZO, LIScO, LIScO-5%, and LINO were synthesized by using a solid-state method. Li_2CO_3 (Alfa Aesar, ACS, 99%min), In_2O_3 (Sigma-Aldrich, 99.998%), TiO_2 (Sigma-Aldrich, 99.5%), $Zr(OH)_4$ (Sigma-Aldrich, 97%), Sc_2O_3 (Sigma-Aldrich, 99.9%), SnO_2 (Sigma-Aldrich, 99.9%), and Nb_2O_5 (Sigma-Aldrich, 99.99%) were used as precursors. For each composition, the precursors were stoichiometrically mixed (except for 10% excess

https://doi.org/10.1021/jacs.5c12231
J. Am. Chem. Soc. XXXX, XXX, XXX−XXX

Li_2CO_3) using a Retsch PM200 planetary ball mill at 250 rpm for 12 h. The precursors were then dried, pelletized, calcined in air at 1050 °C for 4 h, and then air-quenched. For LITO in which the spinel-like phase forms, a second-time sintering with the same heating program was performed to remove the remaining Li_3InO_3-like impurity. The sintered pellets were air-quenched and stored in an Ar-filled glovebox. The powder XRD patterns of the as-synthesized compounds were obtained using a Rigaku MiniFlex 600 diffractometer equipped with a Cu radiation source.

DFT Calculations

We performed spin-polarized DFT[54,55] calculations for evaluating the Li site energies using the Vienna ab initio simulation package (VASP),[56,57] which employs the projector augmented wave[58] potentials. To describe the electronic exchange and correlation, we used the strongly constrained and appropriately normed[59] functional. We expanded the plane wave basis set up to an energy cutoff of 520 eV, sampling only the Γ point within the irreducible Brillouin zone, and utilized a Gaussian smearing (of width 0.05 eV) to integrate the Fermi surface. We used an energy convergence criterion of 10^{-5} eV and a force convergence criterion of |0.03| eV/Å and did not preserve any symmetry to converge all our calculations. We utilized the 'selective dynamics' procedure in VASP, allowing only the proton to move while keeping the rest of the atomic framework fixed (including cell shape and volume). To ensure charge neutrality, we perform all calculations with compensating electrons added as a homogeneous background charge, corresponding to an ideal charge-neutral stoichiometry of $Li_{22}In_{14}O_{32}$ (per conventional cell). We used the pymatgen[60] package to calculate the Ewald energy of the 2 × 2 × 2 domains.

■ ASSOCIATED CONTENT

Supporting Information

The Supporting Information is available free of charge at https://pubs.acs.org/doi/10.1021/jacs.5c12231.

> Elemental analysis, ionic conductivity measurements, single-crystal neutron and X-ray diffraction refinement results, additional Li density distribution analysis, Monte Carlo simulation results, diffuse scattering analysis, Raman spectra, powder synthesis results, and DFT calculations of Li site energies (PDF)

Accession Codes

Deposition Number 2473557 contains the supplementary crystallographic data for this paper. These data can be obtained free of charge via the joint Cambridge Crystallographic Data Centre (CCDC) and Fachinformationszentrum Karlsruhe Access Structures service.

■ AUTHOR INFORMATION

Corresponding Author

Huiwen Ji − *Department of Materials Science and Engineering, University of Utah, Salt Lake City, Utah 84112, United States;* orcid.org/0000-0001-8091-9428; Email: huiwen.Ji@utah.edu

Authors

Yu Chen − *Department of Materials Science and Engineering, University of California Berkeley, Berkeley, California 94720, United States; The Molecular Foundry, Lawrence Berkeley National Laboratory, Berkeley, California 94720, United States;* orcid.org/0000-0002-5420-7571

Caleb Ramette − *Department of Materials Science and Engineering, University of Utah, Salt Lake City, Utah 84112, United States*

Matthew Krogstad − *Advanced Photon Source, Argonne National Laboratory, Lemont, Illinois 60439, United States*

Maxim Avdeev − *Australian Nuclear Science and Technology Organisation, Kirrawee DC, New South Wales 2232, Australia;* orcid.org/0000-0003-2366-5809

Erick Lawrence − *Department of Materials Science and Engineering, University of Utah, Salt Lake City, Utah 84112, United States; Materials Department and Materials Research Laboratory, University of California Santa Barbara, Santa Barbara, California 93106, United States;* orcid.org/0000-0003-0819-1895

Satya Kushwaha − *Department of Chemistry, The Johns Hopkins University, Baltimore, Maryland 21218, United States; Platform for the Accelerated Realization, Analysis and Discovery of Interface Materials (PARADIM), Department of Chemistry, The Johns Hopkins University, Baltimore, Maryland 21218, United States*

Chao-Chun Wei − *Department of Materials Science and Engineering, University of Utah, Salt Lake City, Utah 84112, United States;* orcid.org/0009-0006-1301-1763

Rajavallipuram Sankaran Subramanian − *Department of Materials Engineering, Indian Institute of Science, Bangalore 560012, India*

Birender Singh − *Department of Physics, Boston College, Chestnut Hill, Massachusetts 02467, United States*

Bin Liu − *Department of Materials Science and Engineering, University of Utah, Salt Lake City, Utah 84112, United States*

Xiaoping Wang − *Neutron Scattering Division, Oak Ridge National Laboratory, Oak Ridge, Tennessee 37831, United States;* orcid.org/0000-0001-7143-8112

Christina M. Hoffmann − *Neutron Scattering Division, Oak Ridge National Laboratory, Oak Ridge, Tennessee 37831, United States*

Jue Liu − *Neutron Scattering Division, Oak Ridge National Laboratory, Oak Ridge, Tennessee 37831, United States;* orcid.org/0000-0002-4453-910X

Paul Cardon − *Department of Materials Science and Engineering, University of Utah, Salt Lake City, Utah 84112, United States;* orcid.org/0009-0008-3153-479X

Kenneth S. Burch − *Department of Physics, Boston College, Chestnut Hill, Massachusetts 02467, United States;* orcid.org/0000-0002-7541-0245

Gopalakrishnan Sai Gautam − *Department of Materials Engineering, Indian Institute of Science, Bangalore 560012, India;* orcid.org/0000-0002-1303-0976

Complete contact information is available at: https://pubs.acs.org/10.1021/jacs.5c12231

Author Contributions

‡‡Y.C. and C.R. contributed equally.

Notes

The authors declare no competing financial interest.

■ ACKNOWLEDGMENTS

This work was supported by an NSF Career grant 2145832. Acknowledgement is made to the donors of the ACS Petroleum Research Fund for partial support of this research. This work made use of the bulk crystal growth facility of the Platform for the Accelerated Realization, Analysis, and Discovery of Interface Materials (PARADIM), which is supported by NSF under Cooperative Agreement No. DMR-

2039380. Neutron diffraction measurements used resources at the Spallation Neutron Source, a DOE Office of Science User Facility operated by the ORNL. The authors would like to thank Junhong He for help with sample loading at ORNL, Jacob Phillips and Jared Allred for sharing their DISCUS codes for modification, and Reinhard Neder for guidance on DISCUS use. The elemental analysis employed made use of the shared facilities of the UC Santa Barbara MRSEC (DMR 2308708), a member of the Materials Research Facilities Network. We acknowledge DESY (Hamburg, Germany), a member of the Helmholtz Association HGF, for the provision of experimental facilities. Parts of this research were carried out at PETRA III. Data was collected using P21.1 provided by DESY Photon Science. We would like to thank Oleh Ivashko for assistance during the experiments. Beamtime was allocated for proposal I-20230552.

REFERENCES

(1) Janek, J.; Zeier, W. G. A solid future for battery development. *Nat. Energy* **2016**, *1* (9), 16141.
(2) Janek, J.; Zeier, W. G. Challenges in speeding up solid-state battery development. *Nat. Energy* **2023**, *8* (3), 230−240.
(3) Zhang, Z.; Shao, Y.; Lotsch, B.; Hu, Y.-S.; Li, H.; Janek, J.; Nazar, L. F.; Nan, C.-W.; Maier, J.; Armand, M.; Chen, L. New horizons for inorganic solid state ion conductors. *Energy Environ. Sci.* **2018**, *11* (8), 1945−1976.
(4) Jun, K.; Chen, Y.; Wei, G.; Yang, X.; Ceder, G. Diffusion mechanisms of fast lithium-ion conductors. *Nat. Rev. Mater.* **2024**, *9* (12), 887−905.
(5) Kozinsky, B.; Akhade, S. A.; Hirel, P.; Hashibon, A.; Elsässer, C.; Mehta, P.; Logeat, A.; Eisele, U. Effects of Sublattice Symmetry and Frustration on Ionic Transport in Garnet Solid Electrolytes. *Phys. Rev. Lett.* **2016**, *116* (5), 055901.
(6) Zhou, L.; Assoud, A.; Zhang, Q.; Wu, X.; Nazar, L. F. New Family of Argyrodite Thioantimonate Lithium Superionic Conductors. *J. Am. Chem. Soc.* **2019**, *141* (48), 19002−19013.
(7) Wang, S.; Liu, Y.; Mo, Y. Frustration in Super-Ionic Conductors Unraveled by the Density of Atomistic States. *Angew. Chem., Int. Ed.* **2023**, *62* (15), No. e202215544.
(8) Ji, H.; Urban, A.; Kitchaev, D. A.; Kwon, D. H.; Artrith, N.; Ophus, C.; Huang, W.; Cai, Z.; Shi, T.; Kim, J. C.; Kim, H.; Ceder, G. Hidden structural and chemical order controls lithium transport in cation-disordered oxides for rechargeable batteries. *Nat. Commun.* **2019**, *10* (1), 592.
(9) Lee, J.; Urban, A.; Li, X.; Su, D.; Hautier, G.; Ceder, G. Unlocking the potential of cation-disordered oxides for rechargeable lithium batteries. *Science* **2014**, *343* (6170), 519−522.
(10) Sebti, E.; Evans, H. A.; Chen, H.; Richardson, P. M.; White, K. M.; Giovine, R.; Koirala, K. P.; Xu, Y.; Gonzalez-Correa, E.; Wang, C.; Brown, C. M.; Cheetham, A. K.; Canepa, P.; Clément, R. J. Stacking Faults Assist Lithium-Ion Conduction in a Halide-Based Superionic Conductor. *J. Am. Chem. Soc.* **2022**, *144* (13), 5795−5811.
(11) Kraft, M. A.; Ohno, S.; Zinkevich, T.; Koerver, R.; Culver, S. P.; Fuchs, T.; Senyshyn, A.; Indris, S.; Morgan, B. J.; Zeier, W. G. Inducing High Ionic Conductivity in the Lithium Superionic Argyrodites Li6+xP1−xGexS5I for All-Solid-State Batteries. *J. Am. Chem. Soc.* **2018**, *140* (47), 16330−16339.
(12) Chen, Y.; Lun, Z.; Zhao, X.; Koirala, K. P.; Li, L.; Sun, Y.; O'Keefe, C. A.; Yang, X.; Cai, Z.; Wang, C.; Ji, H.; Grey, C. P.; Ouyang, B.; Ceder, G. Unlocking Li superionic conductivity in face-centred cubic oxides via face-sharing configurations. *Nat. Mater.* **2024**, *23* (4), 535−542.
(13) Chen, Y.; Zhao, X.; Chen, K.; Koirala, K. P.; Giovine, R.; Yang, X.; Wang, S.; Szymanski, N. J.; Xiong, S.; Lun, Z.; Ji, H.; Wang, C.; Bai, J.; Wang, F.; Ouyang, B.; Ceder, G. Coherent-Precipitation-Stabilized Phase Formation in Over-Stoichiometric Rocksalt-Type Li Superionic Conductors. *Adv. Mater.* **2025**, *37*, 2416342.
(14) Lai, W. Transport in Lithium Garnet Oxides as Revealed by Atomistic Simulations. *Annu. Rev. Mater. Res.* **2022**, *52* (1), 305−330.
(15) Kataoka, K.; Akimoto, J. High Ionic Conductor Member of Garnet-Type Oxide Li6.5La3Zr1.5Ta0.5O12. *ChemElectroChem* **2018**, *5* (18), 2551−2557.
(16) He, X.; Zhu, Y.; Mo, Y. Origin of fast ion diffusion in super-ionic conductors. *Nat. Commun.* **2017**, *8* (1), 15893.
(17) Hua, G.; Welberry, T.; Withers, R.; Thompson, J. An electron diffraction and lattice-dynamical study of the diffuse scattering in *β*-cristobalite, SiO2. *J. Appl. Crystallogr.* **1988**, *21* (5), 458−465.
(18) Goodwin, A. L.; Withers, R. L.; Nguyen, H. B. Real-space refinement of single-crystal electron diffuse scattering and its application to Bi2Ru2O7−*δ*. *J. Phys.: Condens. Matter* **2007**, *19* (33), 335216.
(19) Trump, B. A.; Koohpayeh, S. M.; Livi, K. J. T.; Wen, J. J.; Arpino, K. E.; Ramasse, Q. M.; Brydson, R.; Feygenson, M.; Takeda, H.; Takigawa, M.; Kimura, K.; Nakatsuji, S.; Broholm, C. L.; McQueen, T. M. Universal geometric frustration in pyrochlores. *Nat. Commun.* **2018**, *9* (1), 2619.
(20) Booth, C.; Gardner, J.; Kwei, G.; Heffner, R.; Bridges, F.; Subramanian, M. Local lattice disorder in the geometrically frustrated spin-glass pyrochlore Y 2 Mo 2 O 7. *Phys. Rev. B* **2000**, *62* (2), R755.
(21) Thygesen, P. M.; Paddison, J. A.; Zhang, R.; Beyer, K. A.; Chapman, K. W.; Playford, H. Y.; Tucker, M. G.; Keen, D. A.; Hayward, M. A.; Goodwin, A. L. Orbital dimer model for the spin-glass state in Y 2 Mo 2 O 7. *Phys. Rev. Lett.* **2017**, *118* (6), 067201.
(22) Cowley, J. M. X-Ray Measurement of Order in Single Crystals of Cu3Au. *J. Appl. Phys.* **1950**, *21* (1), 24−30.
(23) De Ridder, R.; Van Dyck, D.; Van Tendeloo, G.; Amelinckx, S. A Cluster Model for the Transition State and Its Study by Means of Electron Diffraction. II. Application to Some Particular Systems. *physica status solidi (a)* **1977**, *40* (2), 669−683.
(24) Welberry, T. R.; Weber, T. One hundred years of diffuse scattering. *Crystallogr. Rev.* **2016**, *22* (1), 2−78.
(25) Krogstad, M. J.; Gehring, P. M.; Rosenkranz, S.; Osborn, R.; Ye, F.; Liu, Y.; Ruff, J. P. C.; Chen, W.; Wozniak, J. M.; Luo, H.; Chmaissem, O.; Ye, Z. G.; Phelan, D. The relation of local order to material properties in relaxor ferroelectrics. *Nat. Mater.* **2018**, *17* (8), 718−724.
(26) Weber, T.; Simonov, A. The three-dimensional pair distribution function analysis of disordered single crystals: basic concepts. *Zeitschrift für Kristallographie - Crystalline Materials* **2012**, *227* (5), 238−247.
(27) Barabash, R. I.; Ice, G. E.; Turchi, P. E. *Diffuse Scattering and the Fundamental Properties of Materials*; Momentum press, 2009.
(28) Beyeler, H. U. Cationic Short-Range Order in the HollanditeK1.54Mg0.77T7.23O16: Evidence for the Importance of Ion-Ion Interactions in Superionic Conductors. *Phys. Rev. Lett.* **1976**, *37* (23), 1557−1560.
(29) Seibel, E. M.; Roudebush, J.; Wu, H.; Huang, Q.; Ali, M. N.; Ji, H.; Cava, R. Structure and magnetic properties of the *α*-NaFeO2-type honeycomb compound Na3Ni2BiO6. *Inorg. Chem.* **2013**, *52* (23), 13605−13611.
(30) Mitome, M.; Kohiki, S.; Murakawa, Y.; Hori, K.; Kurashima, K.; Bando, Y. Transmission electron microscopy and electron diffraction study of the short-range ordering structure of *α*-LiFeO2. *Acta Crystallogr., Sect. B:Struct. Sci.* **2004**, *60* (6), 698−704.
(31) Hauck, J. Short-range order and superstructures of ternary oxides AMO2, A2MO3 and A5MO6 of monovalent A and multivalent M metals related to the NaCl Structure. *Acta Crystallographica Section A: Crystal Physics, Diffraction, Theoretical and General Crystallography* **1980**, *36* (2), 228−237.
(32) Deng, Z.; Sai Gautam, G.; Kolli, S. K.; Chotard, J.-N.; Cheetham, A. K.; Masquelier, C.; Canepa, P. Phase behavior in rhombohedral NaSiCON electrolytes and electrodes. *Chem. Mater.* **2020**, *32* (18), 7908−7920.
(33) Sivak, J. T.; Almishal, S. S.; Caucci, M. K.; Tan, Y.; Srikanth, D.; Petruska, J.; Furst, M.; Chen, L.-Q.; Rost, C. M.; Maria, J.-P.; et al.

https://doi.org/10.1021/jacs.5c12231
J. Am. Chem. Soc. XXXX, XXX, XXX−XXX

Discovering high-entropy oxides with a machine-learning interatomic potential. *Phys. Rev. Lett.* **2025**, *134* (21), 216101.
(34) Withers, R. L.; Welberry, T. R.; Larsson, A. K.; Liu, Y.; Norén, L.; Rundlöf, H.; Brink, F. J. Local crystal chemistry, induced strain and short range order in the cubic pyrochlore (Bi1.5−αZn0.5−β)-(Zn0.5−γNb1.5−δ)O(7−1.5α−β−γ−2.5δ) (BZN). *J. Solid State Chem.* **2004**, *177* (1), 231−244.
(35) Deng, Z.; Mishra, T. P.; Mahayoni, E.; Ma, Q.; Tieu, A. J. K.; Guillon, O.; Chotard, J.-N.; Seznec, V.; Cheetham, A. K.; Masquelier, C.; Gautam, G. S.; Canepa, P. Fundamental investigations on the sodium-ion transport properties of mixed polyanion solid-state battery electrolytes. *Nat. Commun.* **2022**, *13* (1), 4470.
(36) Urban, A.; Matts, I.; Abdellahi, A.; Ceder, G. Computational Design and Preparation of Cation-Disordered Oxides for High-Energy-Density Li-Ion Batteries. *Adv. Energy Mater.* **2016**, *6* (15), 1600488.
(37) Nadaud, N.; Lequeux, N.; Nanot, M.; Jové, J.; Roisnel, T. Structural Studies of Tin-Doped Indium Oxide (ITO) and In4Sn3O12. *J. Solid State Chem.* **1998**, *135* (1), 140−148.
(38) Kunz, M.; Brown, I. D. Out-of-Center Distortions around Octahedrally Coordinated d0 Transition Metals. *J. Solid State Chem.* **1995**, *115* (2), 395−406.
(39) Ok, K. M.; Halasyamani, P. S.; Casanova, D.; Llunell, M.; Alemany, P.; Alvarez, S. Distortions in Octahedrally Coordinated d0 Transition Metal Oxides: A Continuous Symmetry Measures Approach. *Chem. Mater.* **2006**, *18* (14), 3176−3183.
(40) Dove, M. T.; Heine, V.; Hammonds, K. D. Rigid unit modes in framework silicates. *Mineral. Mag.* **1995**, *59* (397), 629−639.
(41) Hammonds, K. D.; Dove, M. T.; Giddy, A. P.; Heine, V.; Winkler, B. Rigid-unit phonon modes and structural phase transitions in framework silicates. *Am. Mineral.* **1996**, *81* (9−10), 1057−1079.
(42) Dederichs, P. Diffuse scattering from defect clusters near Bragg reflections. *Phys. Rev. B:* **1971**, *4* (4), 1041.
(43) Petříček, V.; Palatinus, L.; Plášil, J.; Dušek, M. Jana2020 − a new version of the crystallographic computing system Jana. *Zeitschrift für Kristallographie - Crystalline Materials* **2023**, *238* (7−8), 271−282.
(44) Becker, P. J.; Coppens, P. Extinction within the limit of validity of the Darwin transfer equations. I. General formalism for primary and secondary extinction and their applications to spherical crystals. *Acta Crystallographica Section A: Crystal Physics, Diffraction, Theoretical and General Crystallography* **1974**, *30* (2), 129−147.
(45) Momma, K.; Ikeda, T.; Belik, A. A.; Izumi, F. Dysnomia, a computer program for maximum-entropy method (MEM) analysis and its performance in the MEM-based pattern fitting. *Powder Diffr.* **2013**, *28* (3), 184−193.
(46) Momma, K.; Izumi, F. VESTA 3 for three-dimensional visualization of crystal, volumetric and morphology data. *J. Appl. Crystallogr.* **2011**, *44* (6), 1272−1276.
(47) Osborn, R. nexpy/nxrefine. https://github.com/nexpy/nxrefine.
(48) Jennings, G. Crystal coordinate transformation workflow (CCTW). https://sourceforge.net/projects/cctw/.
(49) Arnold, O.; Bilheux, J. C.; Borreguero, J. M.; Buts, A.; Campbell, S. I.; Chapon, L.; Doucet, M.; Draper, N.; Ferraz Leal, R.; Gigg, M. A.; Lynch, V. E.; Markvardsen, A.; Mikkelson, D. J.; Mikkelson, R. L.; Miller, R.; Palmen, K.; Parker, P.; Passos, G.; Perring, T. G.; Peterson, P. F.; Ren, S.; Reuter, M. A.; Savici, A. T.; Taylor, J. W.; Taylor, R. J.; Tolchenov, R.; Zhou, W.; Zikovsky, J. Mantid—Data analysis and visualization package for neutron scattering and μ SR experiments. *Nuclear Instruments and Methods in Physics Research Section A: Accelerators, Spectrometers, Detectors and Associated Equipment* **2014**, *764*, 156−166.
(50) Price-Whelan, A. M.; Sipőcz, B. M.; Günther, H. M.; Lim, P. L.; Crawford, S. M.; Conseil, S.; Shupe, D. L.; Craig, M. W.; Dencheva, N.; Ginsburg, A.; VanderPlas, J. T.; Bradley, L. D.; Pérez-Suárez, D.; de Val-Borro, M.; Aldcroft, T. L.; Cruz, K. L.; Robitaille, T. P.; Tollerud, E. J.; Ardelean, C.; Babej, T.; Bach, Y. P.; Bachetti, M.; Bakanov, A. V.; Bamford, S. P.; Barentsen, G.; Barmby, P.; Baumbach, A.; Berry, K. L.; Biscani, F.; Boquien, M.; Bostroem, K. A.; Bouma, L. G.; Brammer, G. B.; Bray, E. M.; Breytenbach, H.; Buddelmeijer, H.; Burke, D. J.; Calderone, G.; Rodríguez, J. L. C.; Cara, M.; Cardoso, J. V. M.; Cheedella, S.; Copin, Y.; Corrales, L.; Crichton, D.; D'Avella, D.; Deil, C.; Depagne, E.; Dietrich, J. P.; Donath, A.; Droettboom, M.; Earl, N.; Erben, T.; Fabbro, S.; Ferreira, L. A.; Finethy, T.; Fox, R. T.; Garrison, L. H.; Gibbons, S. L. J.; Goldstein, D. A.; Gommers, R.; Greco, J. P.; Greenfield, P.; Groener, A. M.; Grollier, F.; Hagen, A.; Hirst, P.; Homeier, D.; Horton, A. J.; Hosseinzadeh, G.; Hu, L.; Hunkeler, J. S.; Ivezić, Z.; Jain, A.; Jenness, T.; Kanarek, G.; Kendrew, S.; Kern, N. S.; Kerzendorf, W. E.; Khvalko, A.; King, J.; Kirkby, D.; Kulkarni, A. M.; Kumar, A.; Lee, A.; Lenz, D.; Littlefair, S. P.; Ma, Z.; Macleod, D. M.; Mastropietro, M.; McCully, C.; Montagnac, S.; Morris, B. M.; Mueller, M.; Mumford, S. J.; Muna, D.; Murphy, N. A.; Nelson, S.; Nguyen, G. H.; Ninan, J. P.; Nöthe, M.; Ogaz, S.; Oh, S.; Parejko, J. K.; Parley, N.; Pascual, S.; Patil, R.; Patil, A. A.; Plunkett, A. L.; Prochaska, J. X.; Rastogi, T.; Janga, V. R.; Sabater, J.; Sakurikar, P.; Seifert, M.; Sherbert, L. E.; Sherwood-Taylor, H.; Shih, A. Y.; Sick, J.; Silbiger, M. T.; Singanamalla, S.; Singer, L. P.; Sladen, P. H.; Sooley, K. A.; Sornarajah, S.; Streicher, O.; Teuben, P.; Thomas, S. W.; Tremblay, G. R.; Turner, J. E. H.; Terrón, V.; Kerkwijk, M. H. v.; de la Vega, A.; Watkins, L. L.; Weaver, B. A.; Whitmore, J. B.; Woillez, J.; Zabalza, V.; The Astropy Collaboration. The Astropy Project: Building an Open-science Project and Status of the v2.0 Core Package. *Astron. J.* **2018**, *156* (3), 123.
(51) Proffen, T.; Neder, R. B. DISCUS: A program for diffuse scattering and defect-structure simulation. *J. Appl. Crystallogr.* **1997**, *30* (2), 171−175.
(52) Filippova, V.; Kunavin, S.; Pugachev, M. S. Calculation of the parameters of the Lennard-Jones potential for pairs of identical atoms based on the properties of solid substances. *Inorganic Materials: Applied Research* **2015**, *6* (1), 1−4.
(53) Tian, Y.; Reijnders, A. A.; Osterhoudt, G. B.; Valmianski, I.; Ramirez, J.; Urban, C.; Zhong, R.; Schneeloch, J.; Gu, G.; Henslee, I.; et al. Low vibration high numerical aperture automated variable temperature Raman microscope. *Rev. Sci. Instrum.* **2016**, *87* (4), 043105.
(54) Hohenberg, P.; Kohn, W. Inhomogeneous Electron Gas. *Phys. Rev.* **1964**, *136* (3B), B864−B871.
(55) Kohn, W.; Sham, L. J. Self-Consistent Equations Including Exchange and Correlation Effects. *Phys. Rev.* **1965**, *140* (4A), A1133−A1138.
(56) Kresse, G.; Furthmüller, J. Efficient iterative schemes for ab initio total-energy calculations using a plane-wave basis set. *Phys. Rev. B* **1996**, *54* (16), 11169−11186.
(57) Kresse, G.; Hafner, J. Ab initio molecular dynamics for liquid metals. *Phys. Rev. B* **1993**, *47* (1), 558−561.
(58) Kresse, G.; Joubert, D. From ultrasoft pseudopotentials to the projector augmented-wave method. *Phys. Rev. B* **1999**, *59* (3), 1758−1775.
(59) Sun, J.; Ruzsinszky, A.; Perdew, J. P. Strongly Constrained and Appropriately Normed Semilocal Density Functional. *Phys. Rev. Lett.* **2015**, *115* (3), 036402.
(60) Ong, S. P.; Richards, W. D.; Jain, A.; Hautier, G.; Kocher, M.; Cholia, S.; Gunter, D.; Chevrier, V. L.; Persson, K. A.; Ceder, G. Python Materials Genomics (pymatgen): A robust, open-source python library for materials analysis. *Comput. Mater. Sci.* **2013**, *68*, 314−319.

https://doi.org/10.1021/jacs.5c12231
J. Am. Chem. Soc. XXXX, XXX, XXX−XXX